Advanced Powder Materials 3 (2024) 100217

Contents lists available at ScienceDirect

Advanced Powder Materials

journal homepage: www.keaipublishing.com/en/journals/advanced-powder-materials

Nitrogen-doping assisted local chemical heterogeneity and mechanical properties in CoCrMoW alloys manufactured via laser powder bed fusion

Wenting Jiang [a,b], Ruidi Li [a], Junyang He [a], Song Ni [a,*], Li Wang [a,**], Zibin Chen [c], Yi Huang [d,e], Caiju Li [f], Jianhong Yi [f], Min Song [a,***]

[a] State Key Laboratory of Powder Metallurgy, Central South University, Changsha 410083, China
[b] College of Materials and Advanced Manufacturing, Hunan University of Technology, Zhuzhou 412007, China
[c] Research Institute for Advanced Manufacturing, Department of Industrial and Systems Engineering, The Hong Kong Polytechnic University, Hong Kong, China
[d] Department of Design and Engineering, Faculty of Science and Technology, Bournemouth University, Poole, Dorset, BH12 5BB, UK
[e] Materials Research Group, Department of Mechanical Engineering, University of Southampton, Southampton, SO17 1BJ, UK
[f] Faculty of Materials Science and Engineering, Kunming University of Science and Technology, Kunming 650093, China

ARTICLE INFO

Keywords:
CoCrMoW alloy
Laser powder bed fusion
Nitrogen addition
Mechanical properties
Precipitation behaviors

ABSTRACT

CoCrMoW alloys with different nitrogen (N) additions (0, 0.05, 0.1, and 0.2 wt%) were prepared via laser powder bed fusion (LPBF). The effects of N content on the microstructure and mechanical properties were investigated. The results indicate that the LPBFed CoCrMoW alloy with 0.1 wt% N addition (0.1 N alloy) shows the best combination of mechanical properties with a yield strength of ~983 MPa and an elongation of ~19 %. Both the LPBF process and the N addition impose great effects on suppressing the γ to ε martensitic transformation, resulting in a decrease in the width and amount of ε laths/stacking faults. Besides, the N addition promotes the segregation of elements Mo, W, and Si along the cellular sub-grain boundaries (CBs), forming fine and discontinuous precipitates rich in Mo, W and Si along the CBs in the 0.1 N alloy, but dense and continuous $(Mo,W)_5Si_3$ precipitates along the CBs in the 0.2 N alloy. The $(Mo,W)_5Si_3$ precipitates with a tetragonal structure were observed and characterized for the first time in the Co–Cr based alloys. The negative mixing enthalpy between the non-metallic elements N, Si and the metallic elements Mo, W, Cr, and the rapid solidification induced segregation of high melting point elements such as Mo and W along CBs during LPBF process, synergistically contribute to the chemical heterogeneity in the alloys. The pure FCC matrix, the slightly increased segregation of Mo, W, Si elements and fine precipitates along the CBs contribute to the good combination of strength and elongation of the 0.1 N alloy. However, though pure FCC phase was present in the 0.2 N alloy, the dense and continuous $(Mo,W)_5Si_3$ precipitates along CBs acted as nucleation sites for cracks, deteriorating the elongation of the alloy. Overall, it is possible to tune the mechanical properties of the LPBFed CoCrMoW alloy by adjusting the local chemical heterogeneity.

1. Introduction

Cobalt–Chromium–Molybdenum (Co–Cr–Mo) alloys are a kind of common metallic biomaterials and widely used in orthopedic implants due to their excellent combination of corrosion and wear resistance, biocompatibility and mechanical properties [1–4]. The Co–Cr–Mo alloys usually present a dual-phase structure consisting of a hexagonal close-packed phase (ε-HCP phase) and a face-centered cubic phase (γ-FCC phase) [5,6]. The ε phase, a martensitic transformation product [7], is hard and brittle due to less symmetry in lattice compared to the γ phase [8]. Therefore, regulating the features of the two phases (for example the size, volume fraction and morphology) is critical for mechanical performance optimization.

In order to stabilize and increase the volume fraction of the ductile γ phase, adding γ-stabilizing elements (such as Ni, C, and N) to the alloy is one of the effective methods. However, the use of Ni should be avoided as much as possible in terms of biocompatibility since Ni is the most common allergenic metal in the human body [9]. Carbon can also stabilize

* Corresponding author.
** Corresponding author.
*** Corresponding author.
E-mail addresses: song.ni@csu.edu.cn (S. Ni), li.wang@csu.edu.cn (L. Wang), msong@csu.edu.cn (M. Song).

https://doi.org/10.1016/j.apmate.2024.100217
Received 14 May 2024; Received in revised form 2 July 2024; Accepted 3 July 2024
Available online 20 July 2024

the γ phase, but it is easy to form hard and brittle carbides such as $M_{23}C_6$ [10,11]. When coarse $M_{23}C_6$ carbides precipitate along grain boundaries, they may act as nucleation sites and propagation channel for cracks [10, 11]. It has been reported that the addition of N is not only safe for the human body but can also stabilize the γ phase and facilitate the formation of nanoscale Cr_2N precipitates due to the strong affinity between N and Cr, benefiting both the strength and ductility of the material [12]. The nanoscale Cr_2N precipitates act as barriers to partial dislocation slip, affecting significantly the kinetics of the γ to ε martensitic transformation [12]. In addition to the carbides and nitrides, some other secondary precipitates have also been found in the Co–Cr–Mo alloys, including intermetallic compounds σ-phase (CoCr), χ-phase ($Cr_3Co_5Si_2$), Laves phase ($Co_3(Mo,W)_2Si$) [13–15]. Minor elements such as Si, C, N in the alloy influence the stability of the precipitates [14]. The σ-phase precipitates which are well known in Co–Cr–Mo alloys, form along the interdendritic region during solidification or heat treatment, and exist over a wide range of temperatures [1,14]. The χ-phase is formed in the alloys with a relatively high content of Si (≥1.0 wt%) and a low content of C (≤0.2 wt%) [16]. The addition of Si favors the precipitation of the χ-phase instead of the σ-phase. Laves phase $Co_3(Mo,W)_2Si$ was firstly reported in a heat-treated Co25Cr5Mo5W alloy with the addition of 1.0 wt% Si [15]. Furthermore, Lee et al. [17] reported the formation of Mo-concentrated R ($Co_{49}Cr_{21}Mo_{30}$) and μ (Co_7Mo_6) phases in the Co–Cr–Mo alloys with high concentrations of Cr and N. They proposed that the N addition played an important role in impeding the formation of σ-phase due to the preferential interaction between Cr and N. Nonetheless, though N is an essential element for the formation of Cr_2N precipitates and has a strong affinity with Cr, the addition of Si has been reported to suppress the Cr_2N formation as well as the common σ-phase [18]. It is generally challenging to purify Si from metals. Therefore, it is essential to study the effect of simultaneous presence of Si and N on the precipitation of Co–Cr–Mo alloys, which remains unclear. In short, a wide variety of secondary phases have been reported in Co–Cr–Mo alloys. By adjusting the type, size, volume fraction, and distribution of these secondary phases, the mechanical properties of the alloys can be further regulated.

Additive manufacturing (AM) has proposed a feasible alternative for the production of Co–Cr–Mo alloys with a high fraction of the γ phase. The ultrahigh cooling rate (10^5–10^6 K/s) during the AM process helps to retain the high temperature metastable γ phase in the Co–Cr–Mo alloy system [19–21]. Meanwhile, the unique non-equilibrium solidification leads to the formation of metastable cellular structures decorated with elemental segregation/precipitation or dislocation along the cellular boundaries [22–24], which affect significantly the alloy properties. For instance, Zhang et al. [3] prepared a Co–Cr–Mo alloy with a good combination of yield strength (YS) (~594 MPa) and ductility (~19.7 %) by laser powder bed fusion (LPBF), which exhibited a cellular structure with segregation of Cr and Mo along the cell boundaries and the volume fraction of the ε phase is less than 1 %. Roudnicka et al. [1] reported that a large number of stacking faults (SFs) formed in the predominant γ-FCC matrix of a Co–Cr–Mo alloy due to the ultrahigh cooling rates of LPBF, and Mo segregation was observed at the cellular network, which promoted the precipitation of σ-phase during heat treatment. Chen et al. [25] fabricated a Co–Cr–Mo–N alloy by LPBF with a number of nanosized Cr_2N precipitates formed at the cellular boundaries, demonstrating a superior yield strength of ~845 MPa and elongation to fracture of ~12.7 %.

Over the past few decades, various N doping methods have been developed to prepare a *N*-doped Co–Cr–Mo alloys, including: (1) direct addition of nitride such as Cr_2N powders in the melts during casting [26], (2) direct addition of Cr_2N powders by mechanical mixing during powder metallurgy [25], and (3) melting or gas atomization in N_2 atmosphere [27]. In this study, N element was successfully and efficiently added to CoCrMoW alloy powders with consolidated Cr_2N blocks placed at the bottom of the crucible as the N resource and covered with CoCrMoW alloy powders during gas atomization process. The consolidated Cr_2N blocks with a relatively low surface ratio compared with the Cr_2N powders retarded the decomposition of Cr_2N and the evaporation of N_2 at high temperature, benefiting the effective doping of N into the alloy powders. The LPBFed CoCrMoWN alloy with 0.1 wt% N addition exhibited a superior combination of mechanical properties with a yield strength of ~983 MPa and an elongation of ~19 %. Multi-scale characterizations were conducted to reveal the phase composition, elemental segregation and precipitation in the LPBF fabricated alloys with different N contents, as well as their deformation behaviors. The N addition induced local chemical heterogeneity and the corresponding microstructural evolutions and mechanical properties were analyzed in detail. Precipitates $(Mo,W)_5Si_3$ with a tetragonal structure were observed and characterized for the first time in the Co–Cr based alloys, which contribute significantly to the mechanical properties of the alloy.

2. Results

2.1. Mechanical properties

Fig. 1a displays the representative tensile engineering stress-strain curves of the LPBFed CoCrMoWNx alloys with different N contents. Table 1 lists the mechanical properties of the LPBFed alloys. The 0 N alloy achieves a good combination of YS of ~820 MPa and an elongation of ~22 %. Compared to the 0 N alloy, the 0.05 N alloy exhibits a higher YS (~880 MPa) and an elongation of ~21 %. With the increase of N content to 0.1 wt%, the YS increases to ~983 MPa and elongation decreases slightly from ~22 % to ~19 %. When the doping N content increases to 0.2 wt%, the YS increases sharply to ~1190 MPa while the elongation decreases significantly to 4.2 %. Fig. 1b summarizes the YS and elongation values of the CoCrMoWNx alloys in this piece of work as well as those reported in literature [12,25–34]. Obviously, our LPBFed alloys present superior strength-ductility combination than other LPBFed and casted CoCrMo alloys (with/without N addition). It is worth noting that with the increase of N content from 0 to 0.1 wt%, the YS increases and the ductility has only minor reduction. However, the ductility drops significantly when the N content reaches 0.2 wt%. This suggests that combining in-situ N addition and LPBF is an effective pathway to improve the mechanical properties of CoCrMoW alloy and the optimum N addition in this work is 0.1 wt%. Fig. 1c illustrates the true stress-strain curves and strain hardening rate curves of CoCrMoWNx alloys. It shows that the strain hardening abilities of the 0 N and 0.05 N alloys are nearly identical, while those of the 0.1 N and 0.2 N alloys decrease with increasing N content. The strain hardening rate curves indicate that the addition of N resulted in a lower strain hardening rate across the entire strain region. The effect of N addition on mechanical properties and microstructures will be further discussed latter. The inset images Fig. 1a1 and 1a2 are SEM images showing the fracture morphologies of the 0.1 N and 0.2 N alloys after tensile tests. Fig. 1a1 depicts a typical ductile fracture mode based on the prevailed dimples in the 0.1 N specimen. Similar morphologies were also observed in LPBFed 0 N and 0.05 N alloys. However, plenty of cleavage steps (as marked by green arrow) and some tear ridges (as marked by yellow arrow) can be observed in the 0.2 N alloy, as shown in Fig. 1a2, evidencing a brittle fracture mode. This means that with further N addition from 0.1 wt% to 0.2 wt%, the fracture behavior changes from ductile fracture to cleavage fracture, resulting in obvious ductility loss. The fracture behaviors of these alloys are consistent with their tensile ductility.

2.2. Microstructures of the LPBFed CoCrMoWNx alloys

Fig. 2a– h shows the typical EBSD inverse pole figures (IPF) and corresponding phase maps taken from the cross sections (X–Y planes) and the longitudinal sections (X-Z planes) of the LPBF fabricated 0 N and 0.2 N alloys. The EBSD IPF and phase maps of the 0.05 N and 0.1 N alloys are provided as Supplementary Fig. 1 (Fig. S1). It can be seen that all LPBFed CoCrMoWNx alloys show similar average grain sizes without obvious

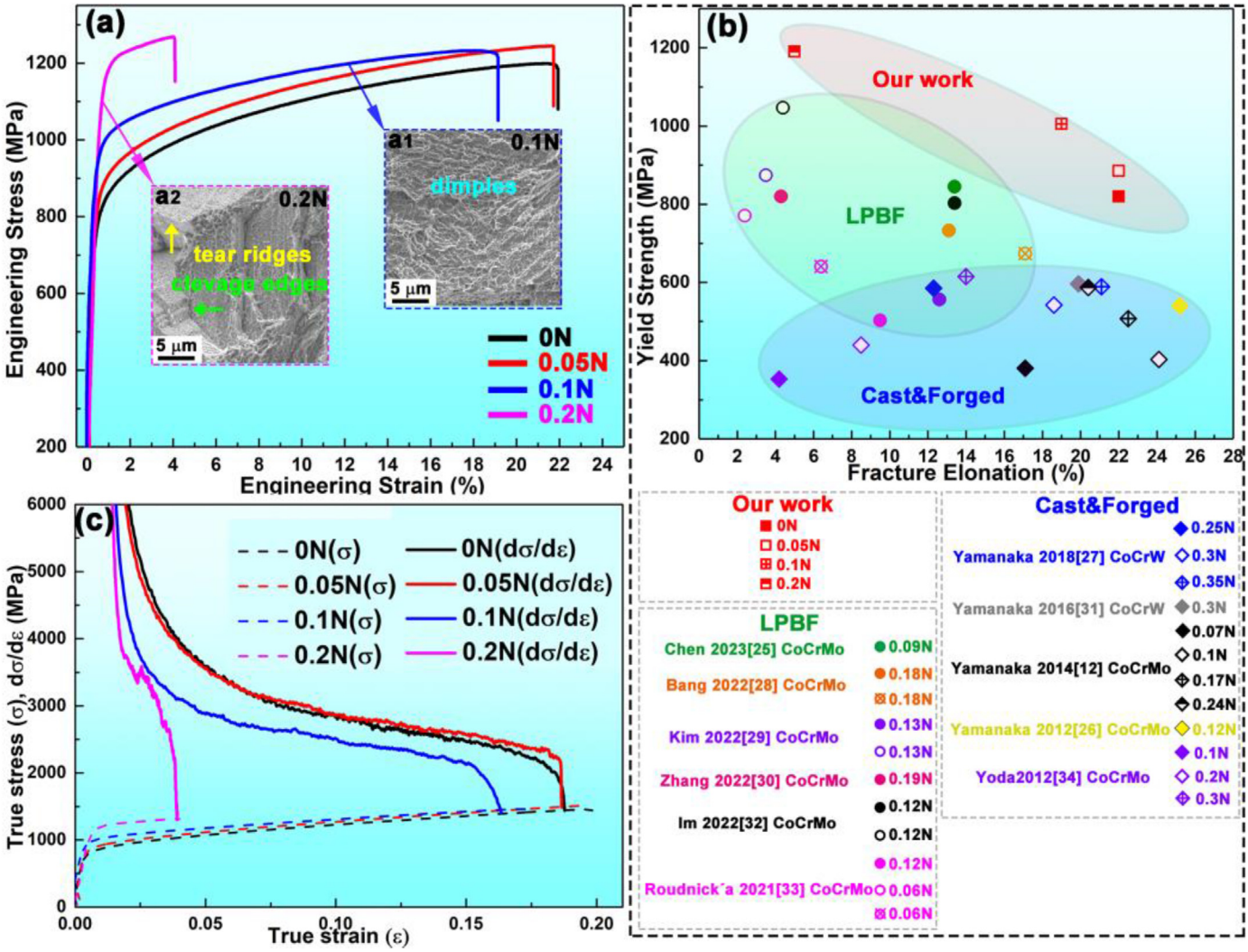

Fig. 1. (a)Tensile engineering stress-strain curves of the LPBFed CoCrMoWN*x* alloys with different N contents, SEM images (a1) and (a2) showing the morphologies of the fracture surfaces of 0.1 N and 0.2 N alloys were inserted; (b) Comparison of the YS and elongation values of the current alloys with those reported in the literature; (c) True stress-strain (σ-ε) curves and strain hardening rate (dσ/dε) curves of the LPBFed CoCrMoWN*x* alloys with different N contents.

Table 1
Mechanical properties of LPBFed CoCrMoWN*x* alloys.

Samples	YS (MPa)	UTS (MPa)	Elongation (%)
0 N	820 ± 20	1185 ± 24	22.3 ± 1.5
0.05 N	880 ± 12	1244 ± 15	21.7 ± 1.0
0.1 N	983 ± 20	1237 ± 10	19.2 ± 0.8
0.2 N	1190 ± 30	1267 ± 35	4.2 ± 0.5

texture viewed on both the X–Y and X-Z planes, which implies that the N addition did not change the grain size of the alloy significantly. The phase maps reveal no noticeable ε phase (green area) detected under EBSD. The grain size distribution histograms and pole figures of the LPBFed CoCrMoWNx alloys, provided in Supplementary Fig. 2 (Fig. S2), further confirm the grain size and texture characteristics. The XRD patterns of CoCrMoWNx alloys with different contents of N are shown in Fig. 2i and j. The 0 N and 0.05 N alloys show mainly the γ-FCC phase and a very little amount of the ε-HCP phase. The volume fractions of γ-FCC and ε-HCP phase can be determined by the method proposed by Sage and Guillaud [2,35]:

$$\mathrm{hcp(wt.\ \%)} = \frac{I(10\bar{1}1)_{hcp}}{I(10\bar{1}1)_{hcp} + 1.5I(200)_{fcc}} \quad (1)$$

where $I(10\bar{1}1)_{hcp}$ and $I(200)_{fcc}$ are the integrated intensities of the $(10\bar{1}1)_{hcp}$ and $(200)_{fcc}$ diffraction peaks for the HCP and FCC phase, respectively. The volume fractions of ε-HCP phase formed in 0 N and 0.05 N alloys were calculated to be ~14 % and 3 %, respectively. With further increase of N content to 0.1 wt % and 0.2 wt %, the $(10\,\bar{1}\,1)\varepsilon$ and $(10\,\bar{1}\,2)\varepsilon$ peaks almost disappear, which means the 0.1 N and 0.2 N alloys are composed of almost the γ-FCC phase. Therefore, the N doping hindered the γ→ε martensitic transformation. Notice that the peaks of the 0.2 N alloy shift to the lower 2θ obviously due to lattice expansion for the addition of nitrogen as shown in Fig. 2j. The lattice parameters of 0 N, 0.05 N, 0.1 N and 0.2 N alloys are calculated to be approximately 3.5803 Å, 3.5823 Å, 3.5862 Å, and 3.5951 Å, respectively, demonstrating crystal lattice expansion with the nitrogen addition. The $(220)_\gamma$ diffraction peak was used for lattice parameter calculation. No diffraction peaks of precipitates were observed from the XRD patterns for all specimens.

The OM and SEM images showing the macro-scale morphologies of the as-built 0 N alloy were presented in the supplementary material as Fig. S3. In Figs. S3a and S3b, flat lath-shaped melt pools and fish-scale-shaped melt pools can be seen on X–Y and X-Z planes, respectively, with the Z direction parallel to the building direction. The SEM images in Figs. S3c and S3d display both cellular sub-grains and columnar sub-grains. Notably, all the LPBFed CoCrMoW alloys with different N

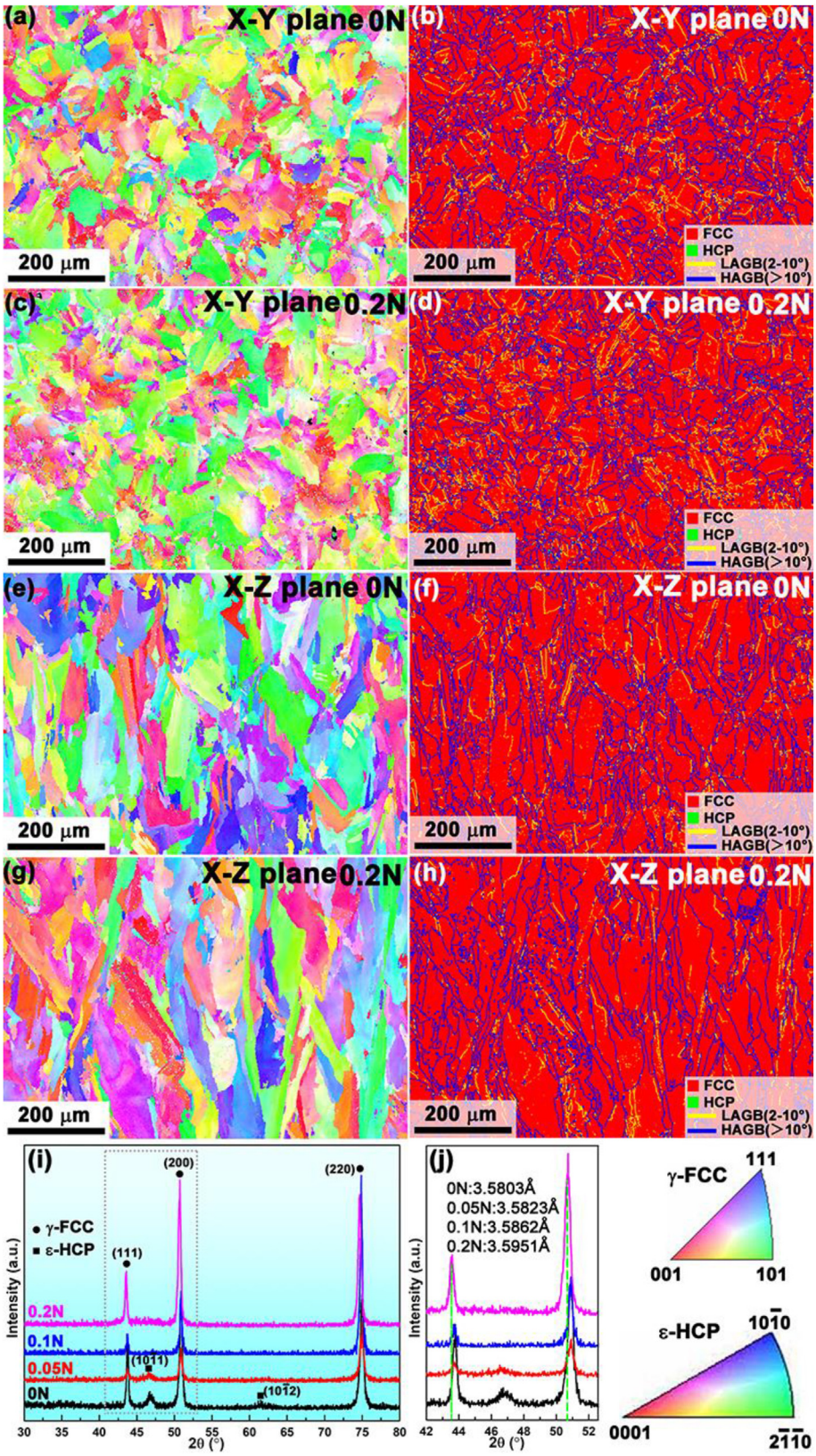

Fig. 2. (a–h) The EBSD inverse pole figures (IPF) and corresponding phase maps taken from the cross sections (X–Y planes) and the longitudinal sections (X-Z planes) of the LPBF fabricated 0 N and 0.2 N alloys; (i, j) The XRD patterns of CoCrMoWN*x* alloys with different N contents.

additions in this study exhibit similar melting pool morphologies, and no obvious macro-scale cracking was observed. To elucidate the influence of nitrogen addition on mechanical properties, comprehensive microstructural characterization was conducted for each sample. Fig. 3a-g shows the microstructures of the 0 N CoCrMoW alloy. Fig. 3a and b are electron channeling contrast (ECC) images, presenting a number of

planar defects (SFs/thin ε) forming networks and a few small precipitates distributed sparsely. Fig. 3c-g are typical HAADF-STEM, EDS mapping, TEM and HRTEM images of the alloy, showing the cellular sub-grains, a few nanoscale precipitates, a high density of SFs and ε laths. As shown in Fig. 3c, some of the dark precipitates were determined to be manganese oxide as impurities in our previous work [36], while the bright precipitates, most of which locate at the triple junctions of the cellular sub-grain boundaries (CBs), were analyzed via EDS mapping. Fig. 3d shows a STEM image and the corresponding EDS mappings of a local area containing CBs and two precipitates. Very weak elemental segregation can be detected along the CBs under TEM, while the two precipitates are more noticeably rich in Mo, W, Si. From Fig. 3e and f, the γ-FCC phase with the {111} plane stacking sequence of … ABCABC … and the ε-HCP phase with the (0001) plane stacking sequence of … ABABAB … were observed. Besides, some SFs also exist in the ε lath. Reversible γ ↔ ε phase transformation can occur via gliding of Shockley partials on every second {111} plane in the γ phase or every second (0001) plane in the ε phase for materials with relatively low stacking fault energy. The FFT image in Fig. 3g shows the orientation between the thin ε lath and γ matrix, which obeys the Shoji-Nishiyama rule: $\{111\}\gamma//(0001)\varepsilon$ and $<\bar{1}\ 10>\gamma//<1\ \bar{2}\ 10>\varepsilon$. The ε-HCP laths can be observed easily under TEM, which is in accordance with the presence of ε-HCP peaks in the XRD pattern, as shown in Fig. 2i. Fig. 3h-n shows the microstructures of the 0.1 N alloy. Fig. 3h is an ECC image and Fig. 3i is a magnified image of the squared area in Fig. 3h. A high density of lamellae can be observed in almost every grain. Fig. 3j-l displays typical HAADF-STEM images of the 0.1 N alloy. Precipitates in spherical shape were observed and some of them were marked with pink arrows in Fig. 3j. Compared with the 0 N alloy, many of the bright precipitates in the 0.1 N alloy were not only distributed at the triple junctions of the CBs but also along the CBs. From Fig. 3k and l, a high density of SFs lying on two groups of {111} planes and much fewer ε thin laths were observed in the 0.1 N alloy compared with the 0 N alloy. This agrees with the XRD pattern of the 0.1 N alloy in Fig. 2i that no obvious ε peaks were detected. The FFT image in Fig. 3m indicates a pure FCC structure with streaking attributed from SFs. The STEM-EDS analysis in Fig. 3n presents that the precipitates along the CBs are obviously rich in Mo, W, Si and the cellular boundary is also slightly rich in Mo, W and Si, while no obvious N segregation was detected.

Fig. 4 shows the microstructures of the 0.2 N alloy. Fig. 4a displays a typical ECC image illustrating the coexistence of cellular and columnar sub-grains. Fig. 4b provides a magnified view of the area highlighted by the square in Fig. 4a. Note that the 0.2 N alloy shows quite different microstructure features compared with the 0 N and 0.1 N alloys. Firstly, the sub-grain boundaries in the 0.2 N alloy are much clearer than those in the 0 N and 0.1 N specimens, which might be due to the much heavier elemental segregation at substructure boundaries. Secondly, much less planar defects were observed in the 0.2 N alloy. To further reveal the structural features and figure out the possible reasons, HAADF-STEM characterizations were conducted on the 0.2 N alloy sample. Fig. 4c is a typical HAADF-STEM image of the specimen, showing quite clear cellular sub-grain boundaries. In order to determine the phase and structure along the cellular boundary, high-resolution HAADF-STEM characterization was conducted. Fig. 4d is an HAADF-STEM image of an area containing both the γ-FCC matrix and the precipitate at the CBs. Fig. 4e is a high-resolution HAADF image taken from the region of interface, showing the different atomic stacking sequences of the γ-FCC matrix and the precipitate. The fast Fourier transformation (FFT) image in Fig. 4f indicates that the precipitate has a tetragonal structure, having a $<110>p//<110>\gamma$, $(1\bar{1}0)\ p//(\bar{1}11)\ \gamma$ orientation relationship to the γ-FCC matrix. The corresponding STEM-EDS mappings and EDS-line analysis shown in Fig. 4g and h indicate that the precipitate is rich in Mo, W and Si. By measuring the lattice spacing values in Fig. 4e and f, the precipitate along CBs can be then determined as $(Mo,W)_5Si_3$. The results in Fig. 4 indicate that the addition of N not only suppressed the formation of ε phase and stacking faults, but also promoted the elemental segregation towards sub-grain boundaries, forming precipitates rich in Mo, W, Si. To further reveal the elemental distribution at atomic scale, especially for the N element, APT tips were lifted out from a region containing cellular sub-grain boundaries in the 0.2 N alloy. It can be seen from the atom maps in Fig. 4i that elements Mo, W, Si and N seriously segregated at a local area. The 1D concentration figure shows that except for the major elements Co and Cr, other elements all present a higher composition in the local area than that in the matrix, especially for Mo. The concentrations of Mo, W, Si and N were measured to be Mo (34.3 at. %, 41.05 wt%), W (15.2 at. %, 34.85 wt%), Si (10.0 at. %, 3.50 wt%), N (14.2 at. %, 2.48 wt%), all of which far exceed the average concentrations in the alloy. Note that the co-segregation of N element with Mo, W and Si was detected under APT but was not observed under TEM, which might due to the track amount of N in the alloy and the insufficient count of the characteristic X-ray of light element during EDX spectrum collection. This will be further discussed in the discussion.

2.3. Microstructures after deformation

Fig. 5a-f shows the EBSD, ECC and TEM images of the 0.1 N alloy after tensile testing. Fig. 5a and b are EBSD IPF and phase maps showing that a large number of ε lamellae formed during deformation. Fig. 5c shows an ECC image with a magnified image of the squared area at the right up corner. A high density of two directional ε lamellae were clearly observed, indicating that γ to ε martensitic transformation dominated the deformation. Fig. 5d displays a bright-field TEM image and the corresponding SAED pattern, showing two directional ε lamellae with a misorientation of 70.5° in the γ-FCC matrix. The orientation relationship between the γ and ε phase is $\{111\}_\gamma//(0001)_\varepsilon$, and $<\bar{1}10>_\gamma//<1\ \bar{2}10>_\varepsilon$. Besides, kinks were observed at the intersections of two directional ε lamellae, leading to a deviation from the original orientation. This was also confirmed by the inserted SAED pattern, which shows a deviation angle of ~10°. Fig. 5e and f shows HRTEM images containing the intersecting areas of two directional ε lamellae. Kinks with deviation angles of ~10° and ~14° were observed. Fig. 5a-f presents the microstructures of the deformed 0.1 N alloy, in which partial dislocations dominate the deformation, resulting in formation of the massive ε phase. Fig. 5g-i shows the EBSD and ECC images of the 0.2 N alloy after tensile testing. Fig. 5g and h shows the EBSD IPF and phase maps, from which very few ε phase was detected. Fig. 5i are ECC images and Fig. 5i1 is a magnified image of the squared area in Fig. 5i. Cracks were observed at the cellular sub-grain boundaries, especially at the large precipitates. It has been reported that areas of stress concentration, such as precipitate/matrix interfaces, can act as initiation sites for cracks [37–39].

3. Discussion

The multi-scale characterization results indicate that the addition of N not only suppressed the formation of ε phase and stacking faults, but also promoted the elemental segregation towards sub-grain boundaries, forming precipitates rich in Mo, W and Si when the addition of N reached a certain amount. The 0.1 N alloy presents increased YS without notable sacrifice in ductility, while the 0.2 N alloy presents a much higher YS but with significant loss in ductility. The effects of N addition on the microstructure and mechanical properties are analyzed in detail in subsections.

3.1. The effect of N on the stacking fault probability

The addition of N stabilized the γ phase by inhibiting the athermal martensitic transformation in the CoCrMoW alloy. The density of planar defects such as stacking faults and ε martensite is closely related to the stacking fault energy (SFE) of the alloy. The significantly low SFE of the current CoCrMoW alloy contributed to the formation of the athermal ε martensite and the high density of stacking faults. With the addition of N,

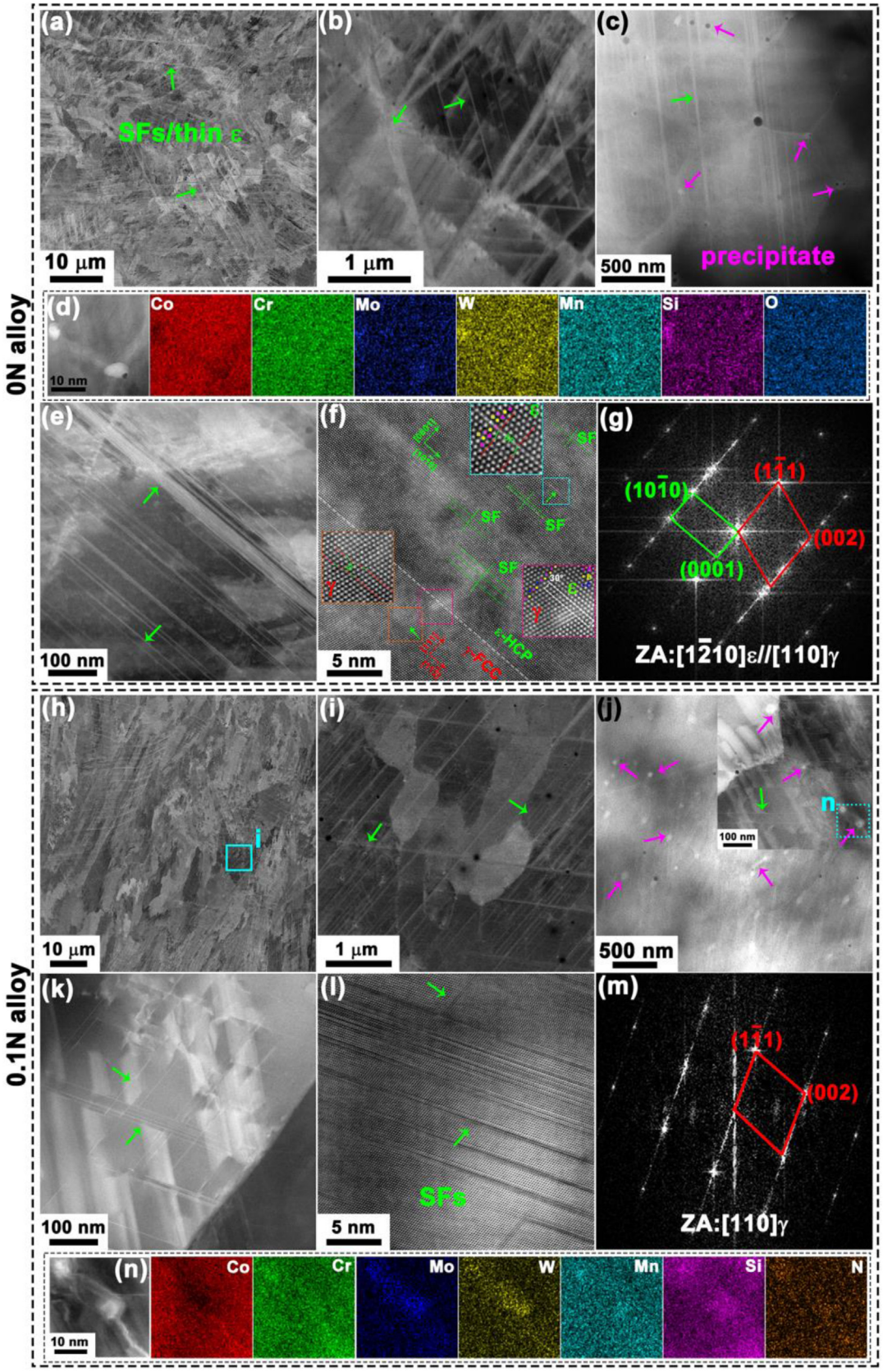

Fig. 3. The microstructures of 0 N alloy: (a, b) the ECC images of 0 N alloy; (c–g) typical HAADF-STEM, EDS mapping, TEM and HRTEM images of the 0 N alloy, showing the cellular sub-grains, a few nanoscale precipitates, a high density of SFs and ε laths. The microstructures of 0.1 N alloy: (h) an ECC image of 0.1 N alloy; (i) a magnified image of the squared area in (h); (j–l) HAADF-STEM images of 0.1 N alloy; (m) FFT image of the area in (l); (n) STEM-EDS mappings showing the element distribution.

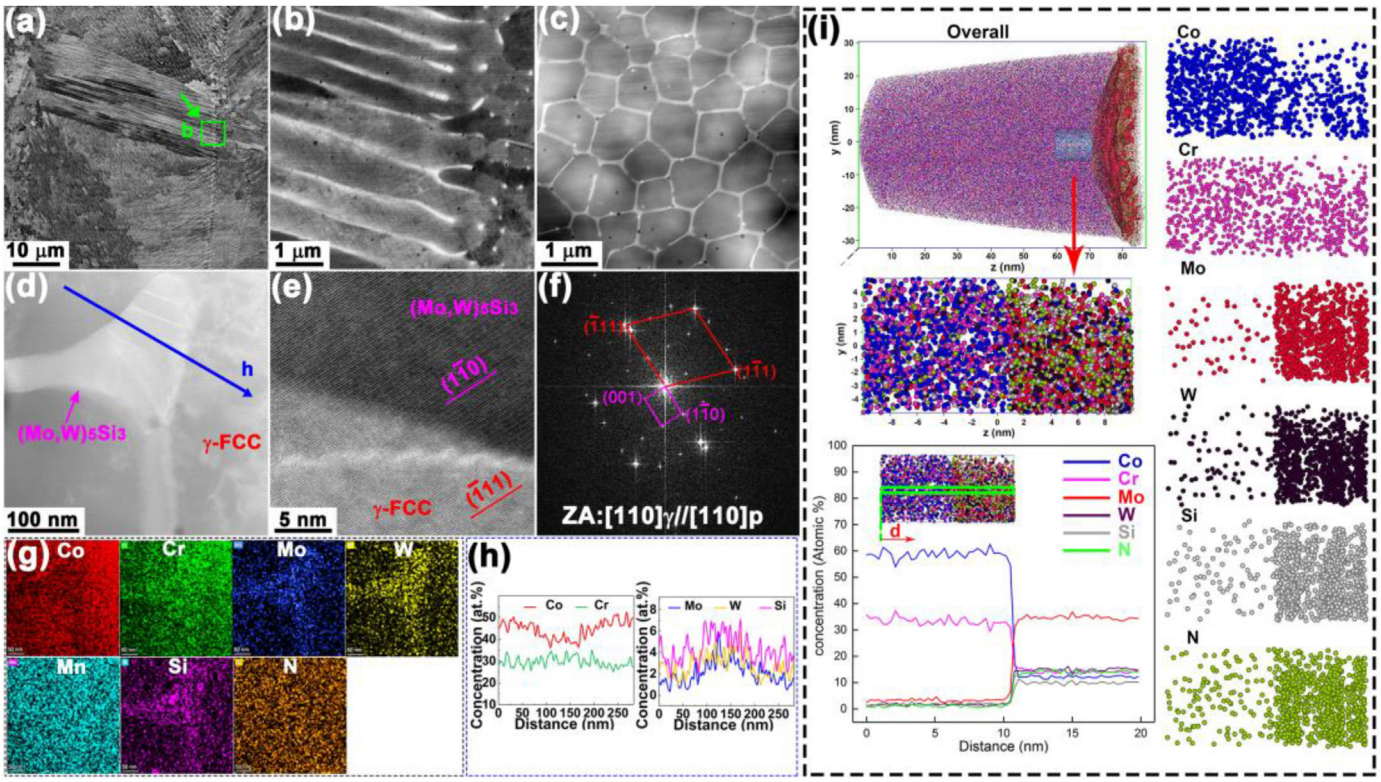

Fig. 4. The microstructures 0.2 N alloy: (a) an ECC image of the 0.2 N alloy; (b) a magnified image of the squared area in (a); (c) a typical HAADF-STEM image showing quite clear cellular sub-grain boundaries; (d) an HAADF-STEM image showing the morphology of precipitate along cellular sub-grain boundary; (e) high-resolution HAADF image taken from the region of interface; (f) FFT image of the area in (e); (g) STEM-EDS mappings of the area in (d); (h) EDS-line analysis along the blue arrow in (d); (i) the APT atom maps and the 1D concentration figure of the 0.2 N alloy showing the element distribution.

the formation of the ε martensite was suppressed, achieving a pure FCC phase in the 0.1 N and 0.2 N alloys. Meanwhile, the number of SFs decreased greatly in the 0.2 N alloy. The effect of N addition on the SFE can be evaluated by calculating the stacking fault probability (SFP), which indicates the formability of stacking faults, on account of that the SFE and SFP have the following relationship [40]:

$$\mathrm{SFE} = \frac{C}{\mathrm{SFP}} \tag{2}$$

Where C is a constant.

The SFP was calculated by the X-ray peak broadening analysis method, with the equations shown as following [41]:

$$\mathrm{SFP} = \frac{a}{1 - \frac{\sqrt{3}}{4}}\left[\left(\frac{1}{D_{\mathrm{eff}}}\right)_{200} - \left(\frac{1}{D_{\mathrm{eff}}}\right)_{111}\right] \tag{3}$$

$$a = \sqrt{3}d_{111} = 2d_{200} \tag{4}$$

$$D_{\mathrm{eff}} = \frac{\lambda}{\beta \cos\theta} \tag{5}$$

where a is the lattice constant, D_{eff} is the mean effective crystallite size, λ is the wavelength of Cu target in XRD, and β is the full width at half maxima. The SFP values of the Co25Cr5Mo5W alloys with different N additions were calculated to be 0.0083 (0 N), 0.0070 (0.1 N), and 0.0062 (0.2 N), as presented in Fig. 6a, together with three schematic images demonstrating the corresponding microstructure features. The addition of N decreases the stacking fault probability, resulting in reduced thickness and number of the ε martensite/stacking faults. Additionally, it is well known that the FCC to HCP martensitic phase transformation can be triggered through Shockley partial dislocation gliding on every second close packed plane and SFs can be regarded as local ε-layers pinning in the FCC matrix [20,42]. Although the solid solubility of N in the CoCrMo alloy is very low [12], the interstitial N atoms, possible nanosized nitrides and short-range orderings in the matrix can inhibit the slip of Shockley partial dislocations [43], impeding the FCC to HCP martensite phase transformation. In this study, an amount of 0.1 wt% N is adequate to achieve a pure FCC phase, which is much less than the amount added in the as-cast alloys [27]. Both the LPBF process with rapid solidification and the N addition contribute to retaining the FCC phase.

3.2. The effect of N addition on the elemental segregation and precipitation

The CoCrMoWNx alloys with different N contents show different elemental segregation and precipitation behaviors. When the N concentration ≤0.1 wt%, the CBs exhibit a slight enrichment in Mo, W and Si. Further increasing the N concentration to 0.2 wt%, a much heavier segregation of Mo, W and Si along the CBs were observed to form $(Mo,W)_5Si_3$ precipitates. The schematic of the formation mechanism of cellular microstructures and element micro-segregation/$(Mo,W)_5Si_3$ precipitates was illustrated in Fig. 6b. A very slight enrichment of Mo, W and Si was detected at the CBs of the 0 N alloy under APT in our previous study [36] but not detected under TEM. When the N concentration increased to 0.1 wt%, some fine and diffusely distributed precipitates rich in Mo, W and Si were observed at the CBs. Further increasing the N concentration to 0.2 wt%, heavier segregation of Mo, W and Si along the CBs were observed forming high density and continuous $(Mo,W)_5Si_3$ precipitates. The possible reasons are as follows: (1) Based on the thermodynamic calculation of the Co–Cr–Mo-xN system [44], the solubility of nitrogen in both γ and ε phases of CoCrMo alloy is very low, which is only 8×10^{-3} or 1×10^{-3} wt% in the γ phase even at high temperature (1473 K or 1273 K) [12]. When the solubility limit of nitrogen concentration is exceeded, the N atoms tend to be ejected into the solid/liquid

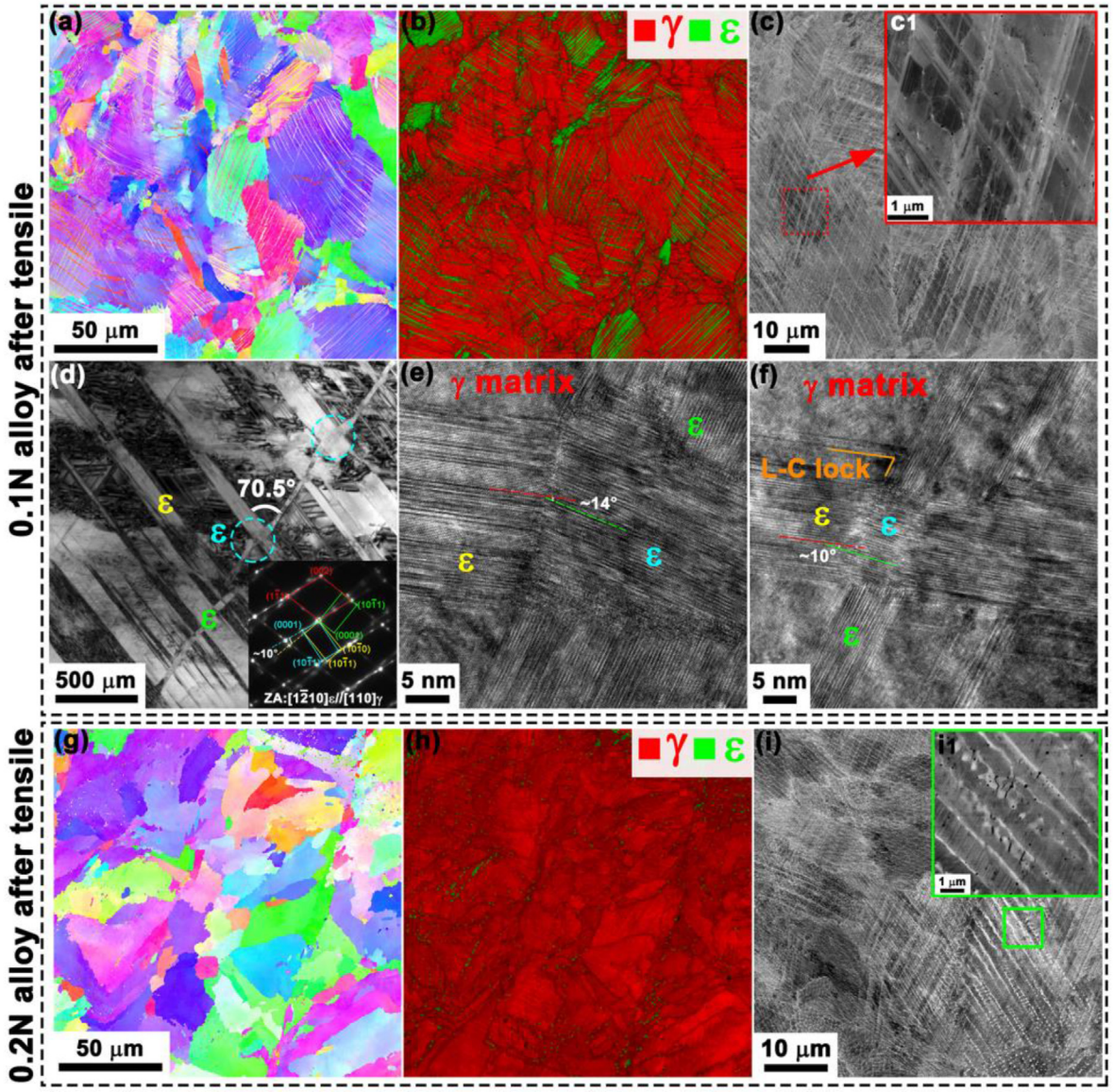

Fig. 5. The microstructures of 0.1 N alloy after tensile testing: (a, b) EBSD IPF and phase maps; (c) ECC image; (d) a bright-field TEM image and the corresponding SAED pattern; (e, f) HRTEM images containing the intersecting areas of two directional ε lamellae. The microstructures of 0.2 N alloy after tensile testing: (g) EBSD IPF map; (h) phase map; (i) ECC images.

interface, i.e., the regions between dendritic arms, as illustrated in Fig. 6b. (2) According to the value of mixing enthalpy between the constituents and N as shown in Table 2 [45], both N and Si show negative mixing enthalpy with the metallic elements. The Mo, W, Cr exhibit more negative mixing enthalpy with N than that of Co, implying that N element has a relatively stronger affinity with Mo, W, Cr than that with Co. In addition, according to the solidification theory, the solvent repels solute atoms with high melting point, such as Mo and W, into the melt at the solid-liquid interface during the cooling process, resulting in micro-segregation of these solute atoms [46]. (3) Though N is an essential element for the formation of Cr_2N precipitates and has a strong affinity with Cr, the presence of Si has been reported to suppress the Cr_2N formation as well as the common σ-phase [18]. Therefore, both the Cr_2N phase and σ-phase were suppressed in this study with the addition of 1.86 wt% Si in the alloy. Attributed to the three reasons mentioned above, the addition of N with the help of Si can pin more Mo and W atoms at cellular sub-grain boundaries, forming $(Mo,W)_5Si_3$ precipitates when the segregation reaches a critical level. The element Si is present in both nitrogen-doped and non-nitrogen-doped samples. However, while Si segregation is not significant in the non-nitrogen-doped samples, its intensification in the nitrogen-doped samples is pronounced, with the degree of segregation increasing with nitrogen concentration. This suggests that nitrogen addition exerts a catalytic-like effect on precipitation. It's noteworthy that the relatively high Si content in the chosen powder determines the type of precipitated phase as Si-rich phase, while the *N*-doping assisted and promoted the precipitation of $(Mo,W)_5Si_3$. The $(Mo,W)_5Si_3$ precipitates with a tetragonal structure were observed and characterized for the first time in the Co–Cr based alloy in this study, which contribute significantly to the mechanical properties.

3.3. The effect of N addition on the mechanical properties

As shown in Figs. 1 and 6, the *N*-free CoCrMoW alloy exhibit a yield strength of ~820 MPa and an elongation of ~22 %, which is attributed to the 3D network constructed by CBs and thin ε laths/SFs offering a decent strengthening contribution, and the FCC phase-based matrix offering a great elongation [36]. Here we discuss the effect of N addition on the mechanical property evolution of the CoCrMoW alloy. With the N

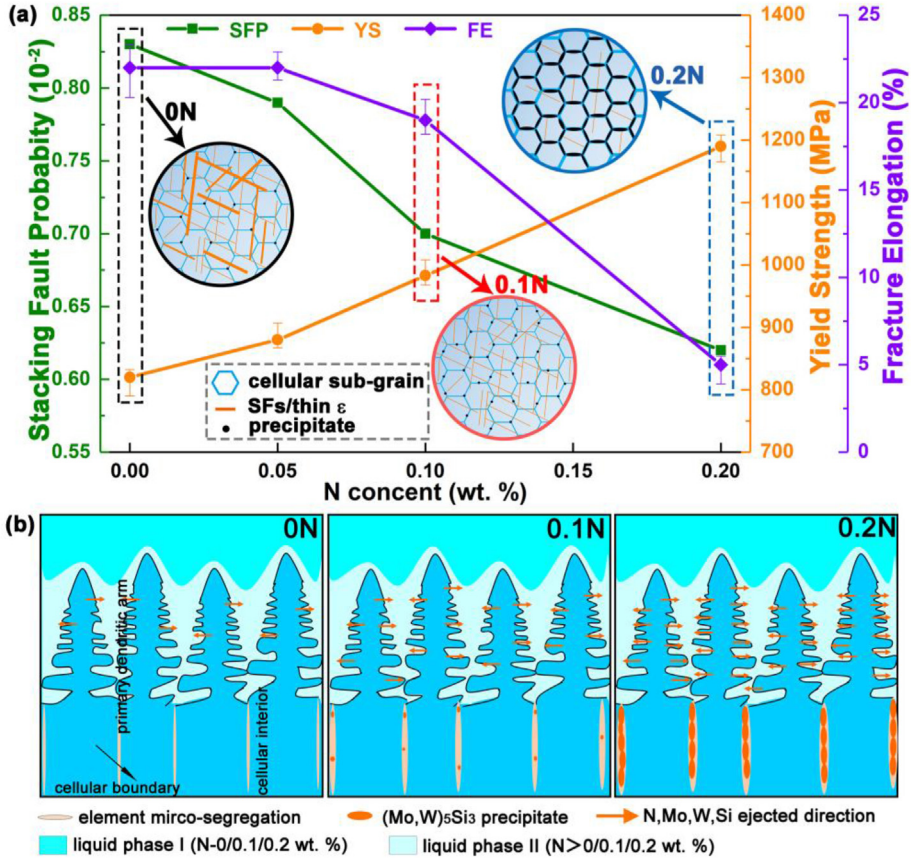

Fig. 6. (a) The SFP values, mechanical properties, and three schematic images demonstrating the microstructure features of the Co25Cr5Mo5W alloys with different N additions; (b) Schematic of the formation mechanism of cellular microstructures and element micro-segregation/$(Mo,W)_5Si_3$ precipitate.

Table 2
The value of mixing enthalpies (KJ/mol) between N with other elements in CoCrMoW alloys [45].

	Co	Cr	Mo	W	Si	N
Co	–	−4	−5	−1	−38	−75
Cr		–	0	1	−37	−107
Mo			–	0	−35	−115
W				–	−31	−103
Si					–	−81
N						–

addition, the yield strength increases to ~983 MPa and 1190 MPa in the 0.1 N and 0.2 N alloys, while the elongation decreased slightly to ~19 % in the 0.1 N alloy but decreased drastically to 5 % in the 0.2 N alloy. The OM and SEM observations indicate that no significant macro-scale cracking occurred in the LPBFed alloys with different N additions. All printed alloys exhibit very high relative densities (>99.0 %). Consequently, the changes in mechanical properties with different N additions are primarily attributed to microstructural evolution induced by N addition. Based on the microstructural characterization of the LPBFed alloys with varying N additions, we discuss the effects of the following factors on mechanical properties: grain size, interstitial N atoms, ε-HCP phase, SFs, CBs and precipitates. Firstly, the CoCrMoWN*x* alloys exhibit similar cellular sub-grain and grain sizes, indicating that the increase in YS with N addition is not due to grain refinement. Secondly, given the quite low solubility of N in the alloy [12,44], the contribution of interstitial N solid solution strengthening to both the 0.1 N and 0.2 N samples should be quite limited. Thirdly, the ε-HCP phase represents a hard and brittle martensitic transformation product, contributing to the alloy's strength. With the addition of N, the formation of the ε martensite was suppressed, achieving a pure FCC phase in the 0.1 N and 0.2 N alloys. This suppression would reduce the material's strength to some extent. Additionally, the number of SFs decreased greatly in the 0.2 N alloy. Dense SFs provide additional resistance to dislocation motion, so their reduction with N addition would also cause some degree of strength reduction. However, such strength reduction is outweighed by other strengthening mechanisms. It is proposed that the segregation of Mo, W, Si at the CBs along with some fine precipitates rich in these elements, strengthens the boundary structure, contributing to the increase in YS in the 0.1 N alloy. CBs as a kind of boundary can impede dislocation movements during deformation [47,48]. The segregation of Mo, W, Si along CBs enhances the hindrance against dislocation penetration. When the N concentration reaches 0.2 wt %, the segregation of Mo, W, Si and N elements at CBs is much more pronounced, forming a high density of precipitates along CBs, which contribute to precipitate strengthening. Compared to the 0.1 N alloy, the 0.2 N alloy exhibits even more pronounced element segregation and precipitation along CBs. As a result, dislocation movement is more restricted in the 0.2 N alloy, leading to a significant increase in strength.

It is well known that plastic deformation is accommodated by slip of dislocations in the Co–Cr based alloys [49,50]. The pure FCC phase of the as-built 0.1 N alloy provides adequate slip systems for Shockley partial dislocation slip to form SFs and ε phase, which contribute to the large elongation of the alloy. However, though pure FCC phase was present in the 0.2 N alloy, the generated high density and continuous $(Mo,W)_5Si_3$ precipitates along CBs are hard and brittle. These precipitates can not only act as obstacles for dislocation motion to raise the YS, but also act as nucleation sites and propagation channels for cracks, deteriorating the elongation of the alloy [51]. In all, by adjusting the local chemical heterogeneity, the mechanical properties of the alloy can be regulated. In this study, the N addition exerts a catalytic-like effect on the precipitation

of the Si-rich phase $(Mo,W)_5Si_3$, which contributes significantly to the mechanical properties of the CoCrMoW alloy.

4. Conclusion

In this work, Co25Cr5Mo5W alloys with high mechanical performance were manufactured successfully by combining LPBF with N addition. The effects of N contents on the microstructure and mechanical properties were investigated. The main conclusions can be drawn as following.

(1) The CoCrMoWN*x* alloys with different N contents show different elemental segregation and precipitation behaviors. When the N concentration is low, such as 0.1 wt%, the CBs exhibit a slight enrichment in Mo, W, and Si. Further increasing the N concentration to 0.2 wt%, heavier Mo, W and Si segregation along CBs were observed, forming $(Mo,W)_5Si_3$ precipitates. The negative mixing enthalpy between the non-metallic elements N, Si and the metallic elements Mo, W, Cr, and the rapid solidification induced segregation of heavy atoms such as Mo and W along CBs during LPBF process, jointly contribute to the chemical heterogeneity in the alloys.

(2) The LPBF CoCrMoW alloy with 0.1 wt % N addition presents the best combined properties with a YS of ~983 MPa and a ductility of ~19 %. The increased YS compared to 0 N CoCrMoW alloy was mainly attributed to the increased segregation of Mo, W, Si along CBs and precipitation strengthening, and the good ductility can be attributed to the pure γ-FCC matrix. With increasing the N addition to 0.2 wt%, the yield strength increased significantly to ~1190 MPa but with great loss in the ductility due to the formation of dense and continuous $(Mo,W)_5Si_3$ precipitates along the CBs.

5. Experiment section

5.1. Materials preparation

The Co25Cr5Mo5WN*x* (x = 0, 0.05, 0.10, 0.20 wt%) alloy powders used in this work were prepared by pre-alloying gas atomization in inert atmosphere to avoid oxidization during atomization. Fig. S4a provides a schematic image presenting the pre-alloying gas atomization with nitrogen doping. The Cr_2N powders consolidated into small blocks were placed at the bottom of the crucible as the nitrogen resource and covered with CoCrMoW alloy powders. The microstructure and particle size distributions of the alloy powders with 0.1 wt% nitrogen doping are shown in Fig. S4b, demonstrating that the powders are of good sphericity and the size distribution of powders is Dv(10)=16.6 μm, Dv(50)=29.3 μm, and Dv(90)=52.3 μm. The X-ray diffraction (XRD) patterns of all powders indicated the predominant γ-FCC phase structure as shown in Fig. S4c and the inset image evidently present that the (111)γ diffraction peak of *N*-doped powders shifts towards lower angles compared with the alloy powders without N doping. The chemical composition of the CoCrMoWN*x* alloy powders was measured by using inductively coupled plasma mass spectroscopy (ICP-MS), as shown in Table 3. Fig. S4d shows the scanning electron microscopy (SEM) - energy dispersive spectrometry (EDS) maps of a *N*-doped particle, presenting homogeneous elemental distribution.

The LPBF process was conducted using an FS271 machine (Farsoon, China) with the following parameters: hatching distance between adjacent laser tracks of 70 μm, scanning speed of 400 mm/s, layer thickness of 30 μm, laser power of 160 W and under the protection of argon atmosphere. The specimens were printed layer-by-layer with the scanning direction alternated by 67° between two adjacent layers, reaching a total height of ~2 mm. The schematic images of the LPBF process and the tensile samples with scanning strategy used in this work are shown in Figs. S1e and S1f, respectively. All printed alloys exhibit very high relative densities (>99.0 %). The compositions of the powders and the specimens after LPBF are presented in Table 3. The Co25Cr5Mo5WNx alloys with different N contents are denoted as 0 N, 0.05 N, 0.1 N and 0.2 N specimens, respectively. Note that there was a decrease in nitrogen content in all LPBFed samples than that in the alloy powders, indicating a slight escape of nitrogen during the LPBF process.

Table 3
The compositions of the powders and the LPBFed alloys (wt. %).

Specimens		Co	Cr	Mo	W	Mn	Si	N
Powders	0 N	Bal.	25.56	5.01	5.6	0.7	1.86	<0.01
	0.05 N	Bal.	25.95	5.04	5.16	0.85	1.66	0.05
	0.1 N	Bal.	26.39	4.98	5.08	0.82	1.70	0.10
	0.2 N	Bal.	27.52	5.02	4.98	0.69	1.58	0.21
LPBF-ed alloys	0 N	Bal.	25.24	5.12	5.26	0.62	1.68	<0.01
	0.05 N	Bal.	26.18	5.01	5.20	0.63	1.66	0.03
	0.1 N	Bal.	26.29	5.04	5.06	0.67	1.52	0.08
	0.2 N	Bal.	27.73	4.99	5.03	0.65	1.46	0.15

5.2. Mechanical properties test

Tensile tests were conducted on an Instron universal testing machine (Instron 5565) with a strain rate of 2×10^{-3} s^{-1} at room temperature, using an optical strain gauge (Instron; AVE 2-2663-901) to measure the strain. All sides of the specimens were carefully polished with SiC sandpaper to remove rough surface before tensile testing. The loading direction is parallel to the substrate and perpendicular to the LPBF building direction. Three parallel specimens of each alloy were tested to ensure the repeatability.

5.3. Microstructural characterization

The constituent phases of powders and LPBFed CoCrMoWNx alloys were identified using X-ray diffractometer (XRD, D/max2550pc) with Cu Kα radiation (wavelength: 1.5418 Å) at a scan rate of 2°/min within the 2θ range of 20°–80°. The microstructures of all specimens were characterized using, scanning electron microscopy (SEM) equipped with electron backscattered diffraction (EBSD) and energy dispersive spectrometry (EDS) detectors (FEI Helios Nano Lab G3 UC), transmission electron microscopy (TEM) and high-angle annular dark field - scanning transmission electron microscopy (HAADF-STEM) (Titan G2 FEI operated at 200 kV, Thermofisher Spectra 300 operated at 300 kV). Specimens for SEM and EBSD observations were prepared by conventional sandpaper grinding and finally polished using 0.02 μm colloidal silica (OP–S). The TSL OIM software was used for EBSD data analysis. TEM foils were mechanically ground using sandpapers to a thickness of ~70 μm, and then twin-jet electro-polished in a mixture of perchloric acid (7 vol %) and alcohol (93 vol%) at a voltage of 30 V and a temperature of −35 °C. Atom probe tomography was conducted for compositional analysis at the atomic scale (APT, LEAP 5000XR) and IVAS software was used for data analysis. The needle-shaped specimens for APT were prepared by the focused ion beam (FIB) lift-out and annular milling method on a dual-beam FIB/SEM instrument.

CRediT authorship contribution statement

Wenting Jiang: Writing – review & editing, Writing – original draft, Methodology, Investigation, Formal analysis, Data curation. **Ruidi Li:** Writing – review & editing, Formal analysis, Data curation. **Junyang He:** Writing – review & editing, Formal analysis. **Song Ni:** Writing – review & editing, Supervision, Project administration, Methodology, Funding acquisition, Formal analysis, Conceptualization. **Li Wang:** Writing – review & editing, Formal analysis, Data curation. **Zibin Chen:** Writing – review & editing, Formal analysis. **Yi Huang:** Writing – review & editing,

Formal analysis. **Caiju Li:** Writing – review & editing, Formal analysis. **Jianhong Yi:** Writing – review & editing, Formal analysis. **Min Song:** Writing – review & editing, Methodology, Formal analysis, Conceptualization.

Acknowledgments

The authors acknowledge the financial support from National Natural Science Foundation of China [grant number 52171130 (S. Ni)], Huxiang Youth Talents Support Program [grant number 2021RC3002 (S. Ni)]. Z.B. Chen would like to acknowledge the financial support from the Research Office and Research Institute of Advanced Manufacturing of the Hong Kong Polytechnic University [grant numbers P0039966 and P0041361]. Y. Huang is grateful for support from the Royal Society in the UK under Grant No. IES\R3\223190.

Appendix A. Supplementary data

Supplementary data to this article can be found online at https://doi.org/10.1016/j.apmate.2024.100217.

References

[1] M. Roudnická, O. Molnárová, J. Drahokoupil, J. Kubásek, J. Bigas, V. Šreibr, D. Paloušek, D. Vojtěch, Microstructural instability of L-PBF Co-28Cr-6Mo alloy at elevated temperatures, Addit. Manuf. 44 (2021) 102025.
[2] Z. Wang, S.Y. Tang, S. Scudino, Y.P. Ivanov, R.T. Qu, D. Wang, C. Yang, W.W. Zhang, A.L. Greer, J. Eckert, K.G. Prashanth, Additive manufacturing of a martensitic Co-Cr-Mo alloy: towards circumventing the strength-ductility trade-off, Addit. Manuf. 37 (2021) 101725.
[3] Y. Zhang, W. Lin, Z. Zhai, Y. Wu, R. Yang, Z. Zhang, Enhancing the mechanical property of laser powder bed fusion CoCrMo alloy by tailoring the microstructure and phase constituent, Mater. Sci. Eng. A 862 (2023) 144449.
[4] T. Mitsunobu, Y. Koizumi, B.S. Lee, K. Yamanaka, H. Matsumoto, Y. Li, A. Chiba, Role of strain-induced martensitic transformation on extrusion and intrusion formation during fatigue deformation of biomedical Co-Cr-Mo-N alloys, Acta Mater. 81 (2014) 377–385.
[5] Z.Y. Chen, C.Q. Lu, Y.H. Zhuo, Z.X. Xia, X. Zhu, C.Y. Wang, Q.B. Jia, Ductility enhancement of additively manufactured CoCrMo alloy via residual stress tailored high stacking fault probability, Scr. Mater. 235 (2023) 115626.
[6] W. Liu, X. An, W. Jiang, S. Ni, M. Song, Microstructural evolution of a polycrystalline cobalt during tensile deformation, Mater. Sci. Eng. A 826 (2021) 141970.
[7] A. Mani, R. Salinas, H.F. Lopez, Deformation induced FCC to HCP transformation in a Co-27Cr-5Mo-0.05C alloy, Mater. Sci. Eng. A 528 (7–8) (2011) 3037–3043.
[8] Y.T. Zhu, X.Y. Zhang, Q. Liu, Observation of twins in polycrystalline cobalt containing face-center-cubic and hexagonal-close-packed phases, Mater. Sci. Eng. A 528 (28) (2011) 8145–8149.
[9] C.N. Kraft, B. Burian, L. Perlick, M.A. Wimmer, T. Wallny, O. Schmitt, O. Diedrich, Impact of a nickel-reduced stainless steel implant on striated muscle microcirculation: a comparative in vivo study, J. Biomed. Mater. Res. 57 (3) (2001) 404–412.
[10] X.P. Tan, P. Wang, Y. Kok, W.Q. Toh, Z. Sun, S.M.L. Nai, M. Descoins, D. Mangelinck, E. Liu, S.B. Tor, Carbide precipitation characteristics in additive manufacturing of Co-Cr-Mo alloy via selective electron beam melting, Scr. Mater. 143 (2018) 117–121.
[11] K. Yamanaka, M. Mori, A. Chiba, Effects of carbon concentration on microstructure and mechanical properties of as-cast nickel-free Co-28Cr-9W-based dental alloys, Mater. Sci. Eng. C 40 (2014) 127–134.
[12] K. Yamanaka, M. Mori, A. Chiba, Effects of nitrogen addition on microstructure and mechanical behavior of biomedical Co-Cr-Mo alloys, J. Mech. Behav. Biomed. Mater. 29 (2014) 417–426.
[13] K. Li, Z. Wang, K. Song, K. Khanlari, X.S. Yang, Q. Shi, X. Liu, X. Mao, Additive manufacturing of a Co-Cr-W alloy by selective laser melting: in-situ oxidation, precipitation and the corresponding strengthening effects, J. Mater. Sci. Technol. 125 (2022) 171–181.
[14] T. Narushima, S. Mineta, Y. Kurihara, K. Ueda, Precipitates in biomedical Co-Cr alloys, Jom 65 (4) (2013) 489–504.
[15] P. Mengucci, G. Barucca, A. Gatto, E. Bassoli, L. Denti, F. Fiori, E. Girardin, P. Bastianoni, B. Rutkowski, A. Czyrska-Filemonowicz, Effects of thermal treatments on microstructure and mechanical properties of a Co-Cr-Mo-W biomedical alloy produced by laser sintering, J. Mech. Behav. Biomed. Mater. 60 (2016) 106–117.
[16] K. Sugawara, Alfirano, S. Mineta, K. Ueda, T. Narushima, Formation of the χ-phase precipitate in Co-28Cr-6Mo alloys with additional Si and C, Metallurgical and, Mater. Trans. 46 (9) (2015) 4342–4350.
[17] S.H. Lee, N. Nomura, A. Chiba, Significant improvement in mechanical properties of biomedical Co-Cr-Mo alloys with combination of N addition and Cr-enrichment, Mater. Trans. 49 (2) (2008) 260–264.
[18] S. Mineta Alfirano, S. Namba, T. Yoneda, K. Ueda, T. Narushima, Precipitates in as-cast and heat-treated ASTM F75 Co-Cr-Mo-C alloys containing Si and/or Mn, Metall. Mater. Trans. A 42 (7) (2011) 1941–1949.
[19] J. Wang, J. Zou, H. Yang, L. Zhang, Z. Liu, X. Dong, S. Ji, Exceptional strength-ductility synergy of additively manufactured CoCrNi medium-entropy alloy achieved by lattice defects in heterogeneous microstructures, J. Mater. Sci. Technol. 127 (2022) 61–70.
[20] B. Wang, X. An, Z. Huang, M. Song, S. Ni, S. Liu, Nitrogen doped Co-Cr-Mo-W based alloys fabricated by selective laser melting with enhanced strength and good ductility, J. Alloy. Compds. 785 (2019) 305–311.
[21] D. Zhang, D. Qiu, M.A. Gibson, Y. Zheng, H.L. Fraser, D.H. StJohn, M.A. Easton, Additive manufacturing of ultrafine-grained high-strength titanium alloys, Nature 576 (7785) (2019) 91–95.
[22] K.G. Prashanth, J. Eckert, Formation of metastable cellular microstructures in selective laser melted alloys, J. Alloy. Compds. 707 (2017) 27–34.
[23] K. Darvish, Z.W. Chen, M.A.L. Phan, T. Pasang, Selective laser melting of Co-29Cr-6Mo alloy with laser power 180-360 W: cellular growth, intercellular spacing and the related thermal condition, Mater. Charact. 135 (2018) 183–191.
[24] T. Zhang, C.T. Liu, Design of titanium alloys by additive manufacturing: a critical review, Adv. Powder Mater. 1 (2022) 100014.
[25] Z. Chen, A. Chen, Q. Jia, Z. Xia, R. Li, C. Wang, J. Pan, Y. Shi, Investigation of microstructures and strengthening mechanisms in an N-doped Co-Cr-Mo alloy fabricated by laser powder bed fusion, Virt, Phys. Prot. 18 (1) (2023) e2219665.
[26] K. Yamanaka, M. Mori, A. Chiba, Enhanced mechanical properties of as-forged Co-Cr-Mo-N Alloys with ultrafine-grained structures, Metall. Mater. Trans. A 43 (2012) 5243–5257.
[27] K. Yamanaka, M. Mori, Y. Torita, A. Chiba, Effect of nitrogen on the microstructure and mechanical properties of Co-33Cr-9W alloys prepared by dental casting, J. Mech. Behav. Biomed. Mater. 77 (2018) 693–700.
[28] G.B. Bang, J.H. Park, W.R. Kim, S.K. Hyun, H.K. Park, T.W. Lee, H.G. Kim, Study on the effect of preheating temperature of SLM process on characteristics of CoCrMo alloy, Mater. Sci. Eng. A 841 (2022) 143020.
[29] K.S. Kim, J.W. Hwang, K.A. Lee, Effect of building direction on the mechanical anisotropy of biocompatible Co-Cr-Mo alloy manufactured by selective laser melting process, J. Alloy. Compds. 834 (2020) 155055.
[30] G.Q. Zhang, J.X. Li, X.Y. Zhou, J. Li, A.M. Wang, Effect of heat treatment on the properties of CoCrMo alloy manufactured by selective laser melting, J. Mater. Eng. Perf. 27 (5) (2018) 2281–2287.
[31] K. Yamanaka, M. Mori, A. Chiba, Developing high strength and ductility in biomedical Co-Cr cast alloys by simultaneous doping with nitrogen and carbon, Acta Biomater. 31 (2016) 435–447.
[32] H.T. Im, D.H. Kim, Y.D. Kim, J.O. Fadonougbo, C.B. Mo, J.Y. Park, K.B. Park, J.W. Kang, H.S. Kang, H.K. Park, Effect of phase transformation on the mechanical properties of the Co-Cr-Mo alloy fabricated by selective laser melting, Mater. Character. 186 (2022) 111767.
[33] M. Roudnická, J. Kubásek, L. Pantělejev, O. Molnárová, J. Bigas, J. Drahokoupil, D. Paloušek, D. Vojtěch, Heat treatment of laser powder-bed-fused Co-28Cr-6Mo alloy to remove its microstructural instability by massive FCC→HCP transformation, Addit. Manuf. 47 (2021) 102265.
[34] K. Yoda, Suyalatu, A. Takaichi, N. Nomura, Y. Tsutsumi, H. Doi, S. Kurosu, A. Chiba, Y. Igarashi, T. Hanawa, Effects of chromium and nitrogen content on the microstructures and mechanical properties of as-cast Co-Cr-Mo alloys for dental applications, Acta Biomater. 8 (2012) 2856–2862.
[35] M. Sage, C. Guillaud, Methode d"analyse quantitative des vari'et'es allotropiques du cobalt par les rayons X, Rev. Metall. 47 (1950) 139–145.
[36] W. Jiang, X. An, S. Ni, L. Wang, J. He, Z. Chen, Y. Huang, M. Song, Achieving excellent strength-ductility combination through the control of intricate substructures in an additively manufactured Co-Cr-Mo alloy, Mater. Sci. Eng. A 886 (2023) 145687.
[37] M. Yang, Y. Wang, R. Ding, Q. Guo, C. Liu, Y. Liu, Precipitates evolution and fracture mechanism of the isothermally solidified TLP bonding joints between 316LN stainless steel and IN718 Ni-based alloy, Mater. Sci. Eng. A 881 (2023) 145440.
[38] Y. Zhang, L. Lan, Y. Zhao, Effect of precipitated phases on the mechanical properties and fracture mechanisms of Inconel 718 alloy, Mater. Sci. Eng. A 864 (2023) 144598.
[39] Z.Z. Jin, M. Zha, S.Q. Wang, S.C. Wang, C. Wang, H.L. Jia, H.Y. Wang, Alloying design and microstructural control strategies towards developing Mg alloys with enhanced ductility, J. Mag. Alloy. 10 (2022) 1191–1206.
[40] S.K. Huang, N. Li, Y.H. Wen, J. Teng, S. Ding, Y.G. Xu, Effect of Si and Cr on stacking fault probability and damping capacity of Fe-Mn alloy, Mater. Sci. Eng. A 479 (2008) 223–228.
[41] Z. Wang, C. Song, Y. Zhang, H. Wang, L. Qi, B. Yang, Effects of yttrium addition on grain boundary character distribution and stacking fault probabilities of 90Cu10Ni alloy, Mater. Charact. 151 (2019) 112–118.
[42] K. Yamanaka, M. Mori, Y. Koizumi, A. Chiba, Local strain evolution due to athermal γ→ε martensitic transformation in biomedical CoCrMo alloys, J. Mech. Behav. Biomed. Mater. 32 (2014) 52–61.
[43] K. Yamanaka, M. Mori, A. Chiba, Nanoarchitectured Co-Cr-Mo orthopedic implant alloys: nitrogen-enhanced nanostructural evolution and its effect on phase stability, Acta Biomater. 9 (4) (2013) 6259–6267.
[44] M. Mori, K. Yamanaka, A. Chiba, Phase decomposition in biomedical Co-29Cr-6Mo-0.2N alloy during isothermal heat treatment at 1073K, J. Alloy. Compds. 590 (2014) 411–416.
[45] A. Takeuchi, A. Inoue, Classification of bulk metallic glasses by atomic size difference, heat of mixing and period of constituent elements and its application to

characterization of the main alloying element, Mater. Trans. 46 (12) (2005) 2817–2829.
[46] M.C. Flemings, Y. Shiohara, Fundamentals of rapid solidification processing, Iron Steel Ind. Jpn. 26 (4) (1986) B126–B130.
[47] J.M. Park, H. Kwon, J. Choe, K.T. Kim, J.H. Yu, Y.U. Heo, H.S. Kim, Cell boundary engineering of ferrous medium-entropy alloy fabricated by laser powder bed fusion, Scr. Mater. 237 (2023) 115715.
[48] H. Jung, J. Lee, G.H. Gu, H. Lee, S.M. Seo, A. Zargaran, H.S. Kim, S.S. Sohn, Multiscale defects enable synergetic improvement in yield strength of CrCoNi-based medium-entropy alloy fabricated via laser-powder bed fusion, Addit. Manuf. 61 (2023) 103360.
[49] I. Weißensteiner, M. Petersmann, P. Erdely, A. Stark, T. Antretter, H. Clemens, V. Maier-Kiener, Deformation-induced phase transformation in a Co-Cr-W-Mo alloy studied by high-energy X-ray diffraction during in-situ compression tests, Acta Mater. 164 (2019) 272–282.
[50] M. Martinez, G. Fleurier, F. Chmelík, M. Knapek, B. Viguier, E. Hug, TEM analysis of the deformation microstructure of polycrystalline cobalt plastically strained in tension, Mater. Charact. 134 (2017) 76–83.
[51] P. Niu, R. Li, Z. Fan, P. Cao, D. Zheng, M. Wang, C. Deng, T. Yuan, Inhibiting cracking and improving strength for additive manufactured Al CoCrFeNi high entropy alloy via changing crystal structure from BCC-to-FCC, Addit. Manuf. 71 (2023) 103584.